Geophys. J. Int. (1992) **111**, 515–530

Thermal convection with non-Newtonian plates

Stuart A. Weinstein[1,2] and Peter L. Olson[1]

[1] *Department of Earth and Planetary Sciences, The Johns Hopkins University, Baltimore, Maryland* 21218, *USA*
[2] *Department of Geological Sciences, University of Michigan, Ann Arbor, Michigan* 48109, *USA*

Accepted 1992 June 13. Received 1992 June 3; in original form 1991 September 19

SUMMARY

The coupling between plate motions and mantle convection is investigated using a fully dynamic numerical model consisting of a thin non-Newtonian layer which is dynamically coupled to a thick Newtonian viscous layer. The non-Newtonian layer has a simple power-law rheology characterized by power-law index n and stiffness constant μ_p. A systematic investigation of steady, single cell configurations demonstrates that under certain conditions ($n > 7$ being one of them) the non-Newtonian layer behaves like a mobile tectonic plate. Time-dependent calculations with multicellular configurations show the ability of the plate–mantle coupling model to adjust the number of plates and their sizes in accordance with the flow in the Newtonian layer. These calculations show that the geometry and number of plates do not necessarily resemble the planform of convection below.

Key words: fully dynamic, mantle, non-Newtonian, plate tectonics, thermal convection, time-dependence.

1 INTRODUCTION

The lithosphere is the top thermal boundary layer of a global system of convection occurring in the Earth's mantle. Due to the thermally activated viscosity of the mantle and the low temperatures at the Earth's surface, the lithosphere acquires mechanical properties which are different from the rest of the mantle. Since the mid 1960s, geophysicists have realized the lithosphere is comprised of several mobile units called plates. Several studies of plate kinematic data show the plates, to a good approximation, behave as rigidly rotating caps except for narrow zones of intraplate deformation at their boundaries (DeMets *et al.* 1990; Minster & Jordan 1978; Chase 1978). This behaviour is fundamentally different from the rest of the mantle, which deforms viscously when stressed over long time-scales. Modelling the behaviour of plates and understanding the interaction between the motion of the plates and convection in the mantle is one of the most important problems in geodynamics. In this paper the results of a systematic numerical study of a new model for plate–mantle coupling are discussed.

Attempts to model the behaviour of plates in a fully dynamic manner have centred on the use of temperature-dependent and non-Newtonian rheology. Davies (1988) examined two-dimensional, time-dependent thermal convection in a fluid with a temperature-dependent viscosity. The idea behind the use of temperature-dependent viscosity is to create a stiff, cold boundary layer like the Earth's lithosphere. However, as Davies (1988) shows, the resulting surface velocity distribution did not resemble that of a mobile, rigid plate. The surface velocity varies sinusoidally across the surface as found for constant viscosity. The problem with temperature dependence is that it stiffens the entire upper boundary layer making it less mobile, but not more plate-like since it fails to concentrate the intraplate deformation into narrow zones. What is needed is a way to weaken the boundary layer in the vicinity of the plate boundaries. Kopitzke (1979), and later Gurnis (1988), Gurnis & Hager (1988), Davies (1989) and King & Hager (1990) show how using *weak zones* (low viscosity regions) at the plate boundaries can mobilize an otherwise stiff plate. Surrounding a highly viscous plate (viscosity is large with respect to underlying fluid) by weak zones can produce velocity profiles like those of the Earth's plates. However, such models are not fully dynamic because they require the specification of weak zones; their size, location and viscosity. Nevertheless, much has been accomplished with such models. Gurnis (1988) introduced the *breakable plate*, in which the plate geometry as well as plate speed is coupled to the flow. The plate breaks when a yield stress criterion is exceeded and two plates combine to form a larger one when they collide. Thus, when a large plate is over an upwelling in the convective flow it will split in two if the stresses generated in the plate are large enough.

Numerical studies by Cserepes (1982), Christensen (1983,

1984), Christensen & Harder (1990), Chen & Morgan (1990) and King & Hager (1990), which examined thermal convection in an infinite Prandtl number, non-Newtonian fluid, show that non-Newtonian rheology can produce plate-like velocity profiles characterized by narrow zones of intraplate deformation and nearly constant velocity elsewhere. Non-Newtonian rheology creates weak zones in regions of high stress and therefore a plate–mantle coupling model based on non-Newtonian rheology can be fully dynamic because it does not require the *ad hoc* assumptions that go with specification of weak zones. Based on this behaviour we have constructed a new plate–mantle coupling model which incorporates the benefits of non-Newtonian rheology.

2 MODEL DESCRIPTION

The plate–mantle coupling model is illustrated in Fig. 1. It consists of a thin non-Newtonian surface layer dynamically coupled to a thick isoviscous, Boussinesq, Newtonian fluid layer. D and h are the constant thicknesses of the Newtonian and non-Newtonian layers respectively and $(h/D) \ll 1$. Except for the difference in rheology, the two layers have identical properties. The Newtonian fluid layer represents the Earth's mantle and the non-Newtonian layer represents the Earth's lithosphere. The non-Newtonian layer deforms in response to the basal shear stress produced by convection in the Newtonian layer. In this model it is assumed that fluid which flows into the non-Newtonian layer becomes non-Newtonian and fluid which flows out of the non-Newtonian layer becomes Newtonian.

3 MODEL EQUATIONS

In our analysis we adopt a coordinate system in which $\hat{z}$ is positive upwards and $\hat{x}$ is positive to the right. The upper surface of the non-Newtonian layer is stress-free and the lower surface experiences tractions σ_{xz}, σ_{zz} produced by convection in the Newtonian layer. Because $(h/D) \ll 1$, the *thin layer* approximation is valid and we need only consider

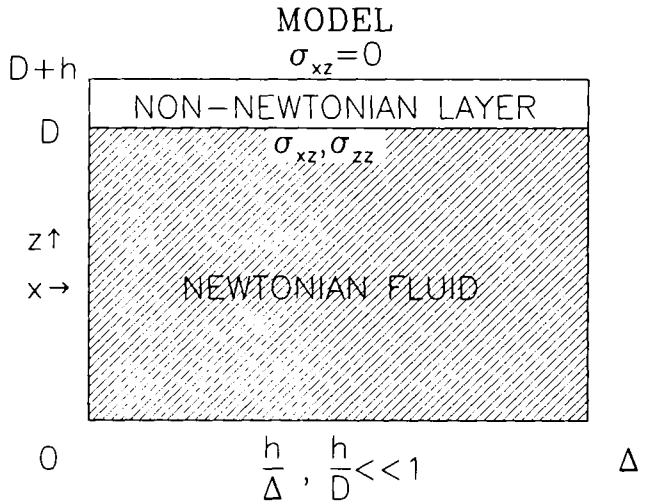

Figure 1. Illustration showing the components of the plate-coupling model.

the force balance in the $\hat{x}$ direction:

$$\frac{\partial \sigma_{xx_p}}{\partial x} + \frac{\partial \sigma_{xz_p}}{\partial z} = 0, \tag{1}$$

subject to the boundary conditions requiring continuity of the vertical normal stress and shear stress at the base of the non-Newtonian layer. These conditions are simply written as

$$\sigma_{xz_p}|_{z=D} = \sigma_{xz_m}|_{z=D}, \tag{2}$$

$$\sigma_{zz_p}|_{z=D} = \sigma_{zz_m}|_{z=D}. \tag{3}$$

In equations (1)–(3), the subscripts p, m denote variables of the non-Newtonian and Newtonian layers respectively. Integrating (1) with respect to z yields

$$\frac{\partial \langle \sigma_{xx_p} \rangle_v}{\partial x} - \frac{\sigma_{xx_p}|_{z=D}}{h} = 0, \tag{4}$$

where

$$\langle \sigma_{xx_p} \rangle_v = \frac{1}{h} \int_D^{D+h} \sigma_{xx_p}\, dz, \tag{5}$$

is the vertically averaged normal stress in the non-Newtonian layer. The non-Newtonian layer is assumed to have a non-Newtonian power-law rheology of the following form:

$$\langle \sigma_{xx_p} \rangle_v = -P_p + \eta_p \frac{\partial u_p}{\partial x}, \tag{6}$$

$$\langle \sigma_{zz_p} \rangle_v = -P_p - \eta_p \frac{\partial w_p}{\partial z}, \tag{7}$$

where the viscosity η is defined as

$$\eta_p = \mu_p (|\langle \sigma^*_{xx_p} \rangle_v| + |\langle \sigma^*_{zz_p} \rangle_v|)^{-(n-1)}. \tag{8}$$

In equations (7) and (8), asterisks denote dimensionless quantities, u_p is the vertically averaged horizontal velocity distribution of the non-Newtonian layer, w_p is the vertical velocity, P is the non-hydrostatic pressure, μ_p is a rheological constant having the dimensions of viscosity and $n = 1, 2, 3, \ldots$ is the power-law exponent. In the limit of Newtonian rheology ($n = 1$), μ_p is twice the Newtonian viscosity. An expression for P_p can be formed from (7) giving

$$P_p = -\sigma_{zz_m} - \eta_p \frac{\partial u_p}{\partial x}, \tag{9}$$

where we made use of incompressibility and substituted $-\partial u_p/\partial x$ for $\partial w_p/\partial z$. In the context of our one-dimensional plate model $\langle \sigma_{zz_p} \rangle_v = \sigma_{zz_m}|_{z=D}$. The constitutive relation (6) can now be written as

$$\langle \sigma_{xx_p} \rangle_v = \sigma_{zz_m}|_{z=D} + 2\eta_p \frac{\partial u_p}{\partial x}. \tag{10}$$

We now non-dimensionalize equations (4) and (10) using a diffusion time-scale,

$$u_p = \frac{\kappa u^*}{D}, \qquad \sigma = \frac{\mu_m \kappa \sigma^*}{D^2}, \qquad \mu_p = \mu_m \mu_p^*, \tag{11}$$

$$h = Dh^*, \qquad L = D\Delta. \tag{12}$$

In these expressions μ_m is the viscosity of the Newtonian layer and κ is the thermal diffusivity. The dimensionless constitutive relation and equation of motion are

$$\langle \sigma^*_{xx_p} \rangle_v = \sigma^*_{zz_m}|_{z^*=1} + 2\eta^*_p \frac{\partial u^*_p}{\partial x^*}, \tag{13}$$

$$\frac{\partial \langle \sigma^*_{xx_p} \rangle_v}{\partial x^*} - \frac{\sigma^*_{xz_p}|_{z^*=1}}{h^*} = 0. \tag{14}$$

Combining (13) and (14) we obtain

$$\omega^*_y|_{z=1} = h^* \left[2\frac{\partial}{\partial x^*}\left(\eta^*_p \frac{\partial u^*_p}{\partial x^*}\right) + \frac{\partial \sigma^*_{zz_m}}{\partial x^*} \right]\Bigg|_{z^*=1}, \tag{15}$$

where ω_y is the vorticity or dimensionless shear stress at the base of the non-Newtonian layer. Equation (15) is a dynamic non-linear boundary condition on the vorticity at the upper boundary of the Newtonian layer and couples the non-Newtonian layer to the convecting flow. [See Ribe (1992) for a derivation of (15) in three-dimensional spherical coordinates.]

The first term in (15) represents the resistance of the non-Newtonian layer to deformation and is the drag that the non-Newtonian layer exerts on the flow. The second term is a driving force which is commonly referred to as the *ridge push* force. The non-Newtonian layer is not explicitly included in the flow. Instead the presence of the non-Newtonian layer is parametrized by (15). This approximation is valid when the non-Newtonian layer is very thin and the mass flux and thermal resistance of the layer is negligible.

4 SOLUTION TECHNIQUE

The entire system of equations and boundary conditions which governs the behaviour of the plate–mantle coupling model are listed below in dimensionless form:

$$\nabla^2 \omega_y = Ra \frac{\partial T}{\partial x}, \tag{16}$$

$$\nabla^2 \psi = -\omega_y, \tag{17}$$

$$\frac{\partial T}{\partial t} + \mathbf{U}_m \cdot \nabla T = \nabla^2 T + \frac{Ra_H}{Ra}, \tag{18}$$

$$\omega_y = 0 \qquad [z = 0], \qquad \psi = 0,$$

$$T = 1, 0 \qquad [z = 0, 1], \tag{19}$$

$$\psi = \omega_y = \frac{\partial T}{\partial x} = 0 \qquad [x = 0, \Delta], \tag{20}$$

$$\omega_y = h\left[2\frac{\partial}{\partial x}\left(\eta_p \frac{\partial u_p}{\partial x}\right) + \frac{\partial \sigma_{zz_m}}{\partial x} \right] \qquad [z = 1], \tag{21}$$

where

$$Ra = \frac{\alpha g\, \Delta T D^3}{\kappa \nu_m}, \qquad Ra_H = \frac{\alpha g C_p H D^5}{\kappa^2 \nu_m}, \tag{22}$$

are the Rayleigh numbers based on the imposed temperature graident and internal heat input. Here, T is temperature, $\mathbf{U}_m$ is velocity field in the Newtonian layer, ψ is the stream function, ω_y is the vorticity, α is the thermal expansivity, g is the acceleration of gravity, C_p is the specific heat, κ is the thermal diffusivity, ν_m is the kinematic viscosity of the Newtonian layer and H is the heat source density. Henceforth, the dimensionless internal heat source Ra_H/Ra will be denoted by the parameter r

The dynamics in the Newtonian layer are governed by equations (16)–(18). These are the governing equations for thermal convection in an isoviscous, infinite Prandtl number, Boussinesq fluid. We have devised a method for solving equations (16)–(21) which requires the reformulation of this system of equations into separate problems which are solved individually and then coupled together in an iterative procedure. The two problems are Newtonian isoviscous, Boussinesq convection beneath a rigid upper surface and a Newtonian viscous, driven cavity flow. This decomposition is allowed due to the linear nature of the assumed Newtonian rheology. The equations which govern convection beneath a rigid boundary are identical to equations (16)–(21), except the non-linear upper boundary vorticity condition is replaced by the no-slip boundary condition which states:

$$u_m|_{z=1} = 0, \tag{23}$$

or that the horizontal velocity component in the Newtonian layer vanishes on the surface. A finite-difference method based on that used by Weinstein, Olson & Yuen (1989) is employed to solve this convection problem. The equations and boundary conditions which govern the behaviour of the driven cavity flow are:

$$\nabla^2 \omega_y = 0, \tag{24}$$

$$\nabla^2 \psi = -\omega_y, \tag{25}$$

$$\psi = \omega_y = 0 \qquad [z = 0], \tag{26}$$

$$u_m|_{z=1} = u_p(x), \qquad \psi = 0 \qquad [z = 1], \tag{27}$$

$$\psi = \omega = 0 \qquad [x = 0, \Delta], \tag{28}$$

where $u_p(x)$ is the velocity distribution of the non-Newtonian layer. This system of equations is also solved using the finite difference method.

Calculation of the velocity field of the non-Newtonian layer begins with the integration of (14), which yields

$$\langle \sigma_{xx_p}(x) \rangle_v - \langle \sigma_{xx_p}(0) \rangle_v = \frac{1}{h}\int_0^x \sigma_{xz_p}(s)|_{z=1}\, ds, \tag{29}$$

where s is a dummy variable in the direction of x. The velocity of the non-Newtonian layer is assumed to be zero at both $x = 0, \Delta$. These conditions on the velocity forbid a net translation of the non-Newtonian layer. Integrating the constitutive equation (9) with respect to x yields:

$$u_p(x) = \frac{1}{2\mu_p}\int_0^x \frac{\langle \sigma_{xx_p} \rangle_v(s) - \sigma_{zz_m}(s)|_{z=1}}{[|\langle \sigma_{xx_p}(s) \rangle_v| + |\sigma_{zz_m}(s)|_{z=1}|]^{-(n-1)}}\, ds \tag{30}$$

The constant of integration must be zero in order to satisfy the condition $u_p|_{x=0} = 0$. Applying the boundary condition $u_p|_{x=\Delta} = 0$ gives

$$\int_0^\Delta \frac{\langle \sigma_{xx_p} \rangle_v(x) - \sigma_{zz_m}(x)|_{z=1}}{[|\langle \sigma_{xx_p}(x) \rangle_v| + |\sigma_{zz_m}(x)|_{z=1}|]^{-(n-1)}}\, dx = 0. \tag{31}$$

With the substitution of (29) into (31) we obtain a condition

for finding $\langle \sigma_{xx_p}(0)\rangle_v$:

$$\int_0^{\Delta} \frac{\left[\langle \sigma_{xx_p}(0)\rangle_v + \frac{1}{h}\int_0^x \sigma_{xz_p}(s)\,|_{z=1}\,ds - \sigma_{zz_m}(x)\,|_{z=1}\right]}{\left[\left|\langle \sigma_{xx_p}(0)\rangle_v + \frac{1}{h}\int_0^x \sigma_{xz_p}(s)\,|_{z=1}\,ds\right| - |\sigma_{zz_m}(x)\,|_{z=1}|\right]^{-(n-1)}} dx = 0 \quad (32)$$

Equation (32) is solved for $\langle \sigma_{xx_p}(0)\rangle_v$ using a first-order Newton–Raphson method. The normal stress distribution is then calculated from (29) and is used in (30) to compute the upper boundary velocity.

The solution procedure within a time step consists of the following steps.

(1) Compute vorticity and streamfunction fields for the current temperature distribution, subject to the no-slip upper boundary condition.

(2) Compute the shear stress (vorticity) on rigid boundary.

(3) Apply the shear stress to the base of the non-Newtonian layer and compute the velocity distribution in the layer.

(4) Compute viscous cavity flow in Newtonian layer using the surface velocity distribution calculated in step (3).

(5) Compute surface shear stress generated by cavity flow.

(6) Add shear stresses computed in steps (2) and (5).

(7) Repeat steps (3)–(6) using shear stresses computed in (6) until changes in the surface velocity distribution are below a specified tolerance.

(8) Combine streamfunctions computed in steps (1) and (4), and use the velocity field from the total streamfunction to advect temperature.

The repetition of steps (3)–(6) allows the flows in the Newtonian and non-Newtonian layers to adjust to one another. The shear stress computed from the rigid upper surface convection problem (step 2) is a first guess for the correct shear stress (vorticity) distribution and is refined by repeating steps (3)–(6), which take into account the motion of the upper boundary and its effects on the upper boundary shear stress.

When steady state results are desired, then this numerical method can be streamlined. In this case, it is not necessary to ensure that the motions of the non-Newtonian and Newtonian layers are coupled at every time step, only at the end of the calculation. Therefore, when computing a steady flow, a large time step is used and steps (3)–(6) are executed only once per time step. In this way the temperature field and the momentum fields of the two layers are relaxed into equilibrium. Time-dependent calculations are computationally expensive and are therefore restricted to low grid densities and Rayleigh numbers. All of the calculations were performed on uniform finite difference grids (Table 1).

Table 1. Gridpoint intervals.

Gridpoint Intervals	Ra
$\frac{1}{30}$	$\leq 5 \times 10^4$
$\frac{1}{70}$	$5 \times 10^4 \leq Ra \leq 5 \times 10^6$
$\frac{1}{100}$	5×10^6

As stated earlier, the Earth's plates generally deform only in narrow zones along their boundaries. One of the goals of this study is to assess the degree to which the surface velocity distributions of the non-Newtonian layer resemble those of the Earth's plates. To accomplish this goal, we have created the diagnostic P called *plateness* which quantifies how plate-like a given surface velocity distribution is. First, we define the quantity P^* as follows

$$P^* = \int_0^{\Delta} \left|\frac{dU^*}{dx}\right| dx, \quad (33)$$

where $U^* = U(x)/\langle U(x)\rangle$ is the velocity normalized by the average velocity. P^* is a measure of the internal deformation in the non-Newtonian layer and does not depend on the average speed of the layer but is sensitive to the distribution of velocity. To show how P^* can discriminate among different velocity distributions we will examine two examples; a sine wave velocity variation with distributed deformation, and a square wave distribution representing ideal plate behaviour where the deformation is confined to infinitesimally thin zones. For the sine wave distribution

$$U(x) = U_0 \sin\left(\frac{\pi x}{\Delta}\right), \quad (34)$$

we obtain

$$U^* = \frac{\pi}{2}\sin\left(\frac{\pi x}{\Delta}\right) \quad (35)$$

and hence for $\Delta = 1$

$$P^* = \frac{\pi^2}{2}\int_0^1 |\cos(\pi x)\,dx)| = \pi. \quad (36)$$

For a square wave velocity distribution periodic in 2Δ such as

$$U(x) = \begin{cases} x = -U_0 & -\Delta < x < 0 \\ x = U_0 & 0 < x < \Delta \end{cases}, \quad (37)$$

P^* is 2. Because the sine wave and square wave characterize poor plate and perfect plate behaviour, respectively, we define P by normalizing P^* for an arbitrary velocity distribution in the following way

$$P = \frac{\pi - P^*}{\pi - 2}. \quad (38)$$

Therefore, in the limit that $P \to 0$ the surface velocity distribution can be characterized as a sine wave (distributed deformation) and in the limit that $P \to 1$ the surface velocity distribution can be characterized as a square wave (perfectly plate-like).

We have also created another diagnostic R, which is simply the ratio of the average velocity in the non-Newtonian layer to the average basal velocity. R is a measure of the difference in mechanical boundary conditions on the upper and lower surfaces of the Newtonian layer. R also gives an indication of how the velocities in the non-Newtonian layer compare to the velocities in the Newtonian layer. In the case where the non-Newtonian layer is so strong that it behaves like a rigid boundary, $R \to 0$. In the opposite limit, where the

non-Newtonian layer is weak and behaves like a stress-free boundary, $R \rightarrow 1$.

5 RESULTS

Over 100 numerical simulations were performed in an effort to understand the behaviour of the plate–mantle coupling model. The Rayleigh numbers considered ranged from 2×10^4 to 5×10^6 and the power-law exponents were varied from 3 to 19. Fortunately, only a few of them need to be presented in detail to illustrate the basic physics of the plate–mantle coupling model. We will first present the results of steady state calculations obtained in the absence of the ridge push force (i.e. $\sigma_{zz_m}|_{z=1} = 0$) and internal heat generation. Later, the effects of internal heat generation and the ridge push force are discussed and finally a few of the results of non-steady calculations are presented. In this way, we can ascertain what the effects of the ridge push force are and under what circumstances do they become important. The thickness of the non-Newtonian layer h is assumed to be 0.01, which in dimensional form is 28.8 km, for all of the calculations. The variable parameters which govern the dynamics of the plate–mantle coupling model are now, Ra, n, μ_p, r and Δ.

5.1 Steady solutions in the absence of the ridge push force

When $\sigma_{zz_m}|_{z=1} = 0$ the dynamic vorticity boundary condition (15) becomes

$$\omega_y(x)|_{z=1} = \frac{h}{n}(2\mu_p)^{1/n}\left(\frac{\partial u_p}{\partial x}\right)^{1/n}\left(\frac{\partial u_p}{\partial x}\right)^{-1}\frac{\partial^2 u}{\partial x^2}. \tag{39}$$

There are two important facts which can be determined from the physics of equation (39) just by inspection. The product of the first four terms in (39) is positive non-definite, therefore, the sign of the vorticity at a point on the base of the non-Newtonian layer is the same as the sign of the curvature of the velocity profile (intraplate deformation) at that point. The product $h(2\mu_p)^{1/n}$ is a dimensionless constant which parametrizes the stiffness of the non-Newtonian layer. This product shows that the layer thickness can trade off with the rheological constant and it is only necessary to specify the values of this product rather than specifying h and μ_p individually.

5.1.1 Surface velocity distributions $\Delta = 1$

Figs 2–5 show the surface velocity distributions obtained from simulations in a square box for several combinations of Ra, n and μ_p. Each figure contains up to four plots, which differ only in the value of μ_p. The information presented above each plot consists of values for three dimensionless constants; the common logarithm of μ_p and the diagnostics R and P. In Fig. 2, four surface velocity distributions are shown for $Ra = 5 \times 10^4$ and a modest power-law exponent of 3. As the rheological constant μ_p is increased, strengthening the non-Newtonian layer, R decreases and P increases. This relationship between P, R and μ_p is independent of the values of Ra and n. R decreases because the non-Newtonian layer becomes less mobile. At this low value of n, none of

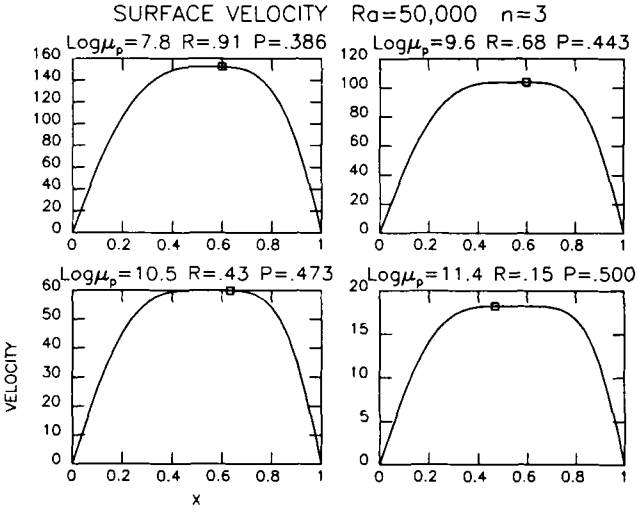

Figure 2. Surface velocity (Peclet number) distributions for $Ra = 50\,000$ and a power-law exponent of 3. X is the dimensionless distance across the non-Newtonian layer. $X = 1$ corresponds to a distance of 2880 km. A dimensionless velocity of 100 scales to 0.1 cm yr^{-1}.

the surface velocity distributions shown in Fig 2 closely resemble a square wave and are therefore not plate-like. This is also indicated by the values of P which do not exceed 0.5 for any of the velocity distributions shown here. However, in Fig. 3, where $n = 19$, there is significant improvement towards plate-like behaviour of the non-Newtonian layer. In fact for the calculation with the highest value of μ_p, $P = 0.812$ and most of the non-Newtonian layer is moving at a constant velocity. For this case, the motion of the non-Newtonian layer is very slow with respect to the underlying convection as indicated by the small value of R. By comparing Figs 2 and 3 it becomes obvious that for given values of Ra and R (assuming R could be specified *a priori*) better plateness is obtained for larger n. As n and μ_p are increased the central portion of the non-Newtonian layer becomes proportionally stronger than its margins near the

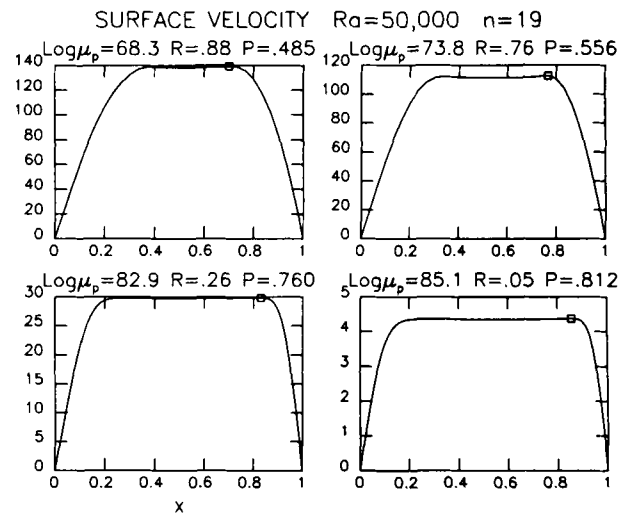

Figure 3. Surface velocity distributions for $Ra = 50\,000$ and a power-law exponent of 19. Note the larger values of plateness which occur for this value of n.

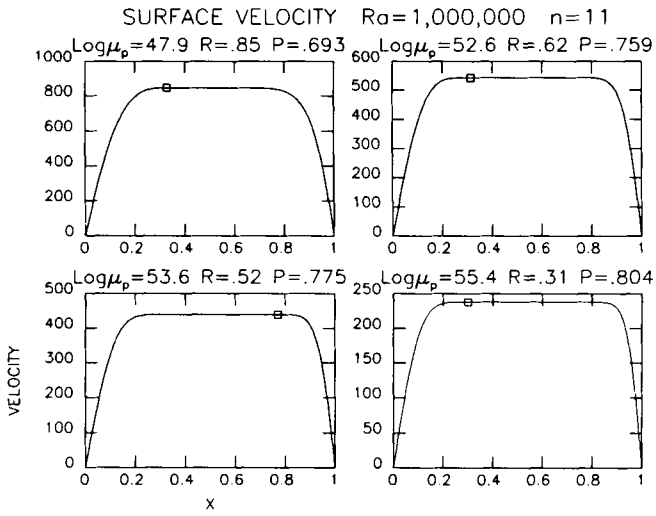

Figure 4. Surface velocity distributions for $Ra = 1\,000\,000$ and a power-law exponent of 11. A dimensionless velocity of 1000 scales to 1.1 cm yr^{-1}.

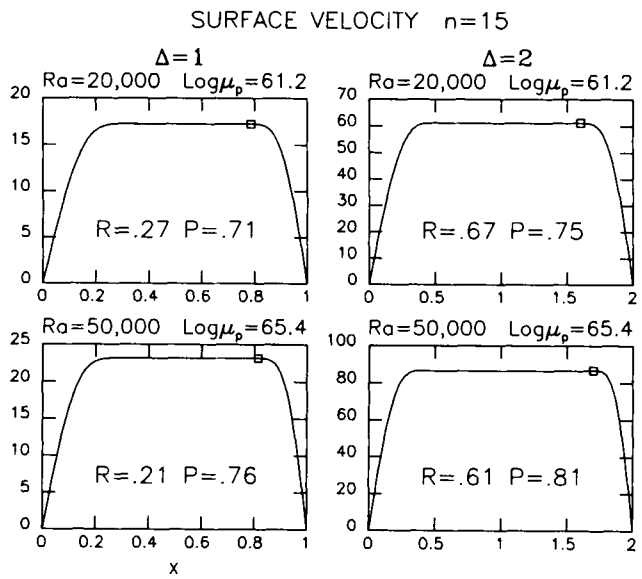

Figure 6. The effects of aspect-ratio on the surface velocity distribution. Greater velocities and better plate-like characteristics are obtained in the non-Newtonian layer with larger aspect-ratio when *Ra* and the rheology are held fixed.

boundaries, resulting in the formation of weak zones. The better values of plateness achieved with larger n indicate that the weak zones become thinner with increasing n. In the limit $n \to \infty$, the weak zones will become infinitesimally thin. Therefore, the rigid-perfectly plastic rheology is the very large n limit of the non-Newtonian rheology used in this model.

Increasing the value of *Ra* to 1×10^6, we find the surface velocity distributions shown in Fig. 4 that have values of $R > 0.5$ for large values of plateness. In this case n is only 11. Fig. 5 shows two surface velocity distributions for $Ra = 5 \times 10^6$ and $n = 11$. The surface velocity distribution in the left plot has better plateness than any distribution shown in 4 for $Ra = 1 \times 10^6$, yet R is more than double. From these results one can see that the model becomes more successful in producing mobile plates at higher Rayleigh numbers. This is important since plate speeds are likely to be characteristic of flow speeds in the mantle. At large values of *Ra* ($\geq 1 \times 10^6$) plate-like velocity distributions in the non-Newtonian layer can be obtained with smaller values of n than at lower values of *Ra*.

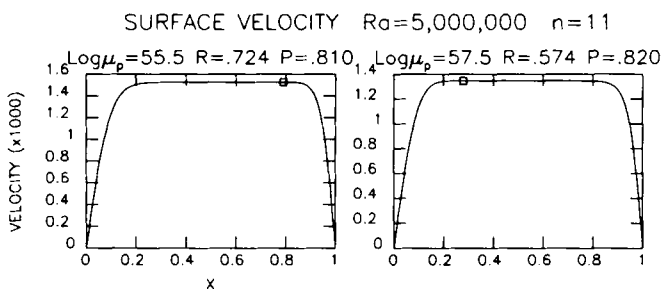

Figure 5. Surface velocity distributions for $Ra = 5\,000\,000$ and a power-law exponent of 11. Note that with the same power-law, our model can generate greater velocities and better plate-like characteristics in the non-Newtonian layer for larger Rayleigh numbers.

5.1.2 *Surface velocity distributions ($\Delta = 2$)*

The effects of increasing the aspect-ratio while the rheology of the non-Newtonian layer and the Rayleigh number are held fixed are shown in Fig. 6. Results are presented only for low values of *Ra* since solutions for steady large aspect-ratio cells could not be obtained for higher values. Increasing the aspect-ratio results in a greatly increased value of R while the plateness only rises slightly. The widths of the deformation zones remain nearly the same, but the velocities in the non-Newtonian layer increase. Therefore in larger aspect-ratios ($\Delta \geq 2$), solutions with mobile plates can be obtained even at low values of *Ra*.

5.1.3 *Normal and basal shear stress distributions ($\Delta = 1$)*

Fig. 7 shows the normal stress distributions in the non-Newtonian layer obtained for $Ra = 1 \times 10^6$ and power-law exponents of 3 and 11 respectively. In the Newtonian layer upwelling flow and downwelling flow occur on the left and right sides of the cell respectively. Therefore, it is evident that the non-Newtonian layer is in tension over the upwelling and in compression over the downwelling. The transition from tension to compression always occurs near the middle of the cell. As μ_p is increased the normal stress distribution becomes nearly linear over most of the cell and the magnitudes of the maximum compressive and tensile stresses increase because the non-Newtonian layer becomes stronger and is able to support a higher level of stress. The magnitudes of the maximum compressive and tensile stresses are nearly equal with the magnitude of the maximum compressive stress being slightly larger than the magnitude of the maximum tensile stress. A dimensionless stress of 10^5 corresponds to 0.3 kb, assuming values of 2.88×10^8 cm, 0.01 cm^2 s^{-1}, and 2.5×10^{21} Pa s for the dimensional parameters, D, κ and μ_m respectively. Thus, at

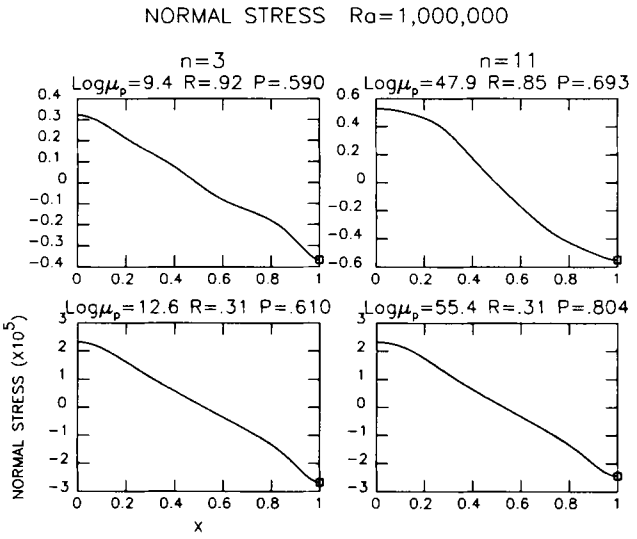

Figure 7. Dimensionless normal stress distributions in the non-Newtonian layer obtained for $Ra = 1\,000\,000$ for power-law exponents of 3 and 11. For each power-law, the normal stress distributions are shown for a fast and slow moving plate. A dimensionless stress of 10^5 scales to 0.3 kb.

$Ra = 10^6$, the in-plate peak normal stresses range from 0.1 kb for the fast moving plates ($R = 0.92$, 0.85) to 0.7 kb for the slower plates ($R = 0.31$).

Fig. 8 shows the shear stress distributions from which the normal stress distributions in Fig. 7 were calculated. Note that the shear stresses are always negative except at the boundaries where they are zero. This behaviour is expected, given the form of equation (39). In order to produce a positive shear stress, the non-Newtonian layer must drive the flow. Since the ridge push force, which is the only internal source of momentum for the non-Newtonian layer, is assumed to be zero the non-Newtonian layer can never drive the flow. All of the velocity distributions found for the steady, single cell calculations are therefore characterized by

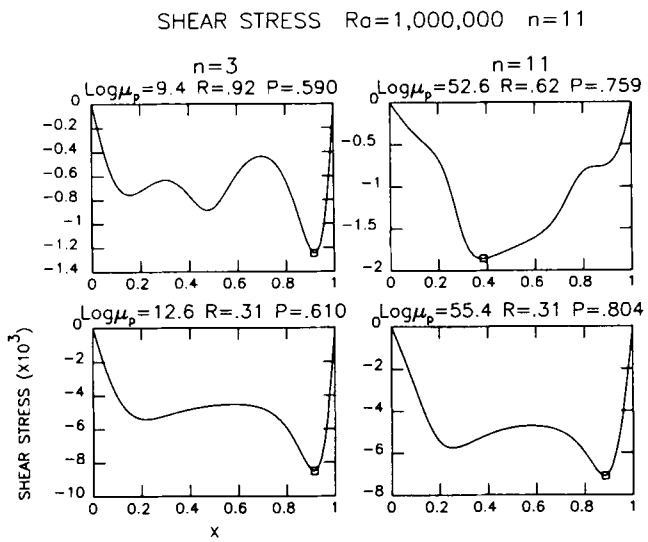

Figure 8. Dimensionless basal shear stress distributions from which the normal stress distributions in Fig. 7 were calculated. A dimensionless stress of 10^3 scales to 0.003 kb.

negative curvature everywhere except at the boundaries where reflection conditions are enforced. The shear stress distribution is unimodal for the lowest value of μ_p and becomes bimodal as μ_p is increased. When μ_p is small, only the central regions of the non-Newtonian layer are sufficiently strong enough to support a large shear stress. As μ_p increases this region broadens and becomes double peaked. The peaks are related to the sharp increase in curvature of the surface velocity distributions (with large plateness) that occurs near the boundaries. The maximum shear stresses on the base of the plate are about 0.015 kb.

5.1.4 *Surface heat flow ($\Delta = 1$)*

Plots of the surface Nusselt number distribution are shown in Figs 9 and 10 for different values of Ra and n. The principal effect of increasing Ra is to increase the heat flow. At $Ra = 1 \times 10^6$, the surface heat is approximately 2.5 times that at $Ra = 5 \times 10^4$ for calculations with similar values of R. It is obvious from Figs 9 and 10 that the heat flow increases with R. There are also subtle differences in the geometry of the heat flow curves themselves. For $Ra = 5 \times 10^4$ the heat flow curves are approximately linear. However, at $Ra = 1 \times 10^6$, the heat flow curves are distinctly different from linear. They all show the heat flow decreasing fairly rapidly near the left boundary and levelling off near the centre of the cell. The dashed lines in Fig. 10 show the heat flow plot function of $\sqrt{(x)}$. In general these curves obey the $\sqrt{(\text{age})}$ relation observed for oceanic lithosphere (Parsons & Sclater 1977), except near the boundaries.

5.1.5 *Structure of convection in the Newtonian layer ($\Delta = 1$)*

Figs 11 and 12 show temperature and streamfunction fields respectively for six calculations peformed with the same values of Ra and n but with differing values of μ_p. The streamline and temperature contour intervals are the same for all of the streamfunction and temperature fields. The effects of increasing μ_p (decreasing surface mobility) on the temperature and streamfunction fields are immediately noticeable. As the non-Newtonian layer becomes rigid and

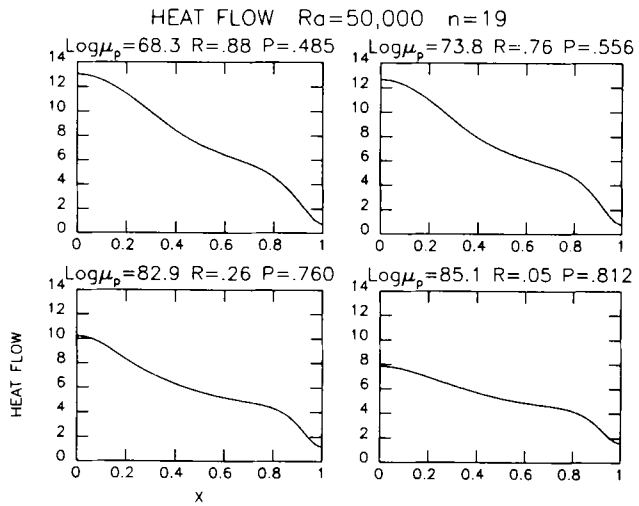

Figure 9. Surface heat flow (surface averaged Nusselt number) for $Ra = 50\,000$ and a power-law exponent of 19.

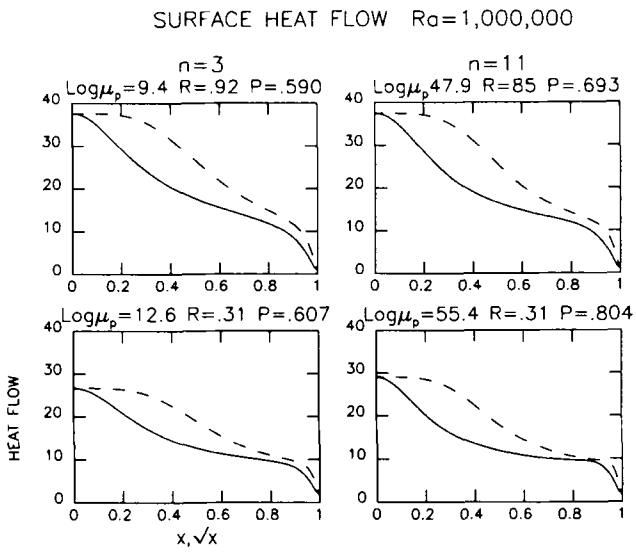

Figure 10. Surface heat flow (surface averaged Nusselt number) for $Ra = 1\,000\,000$ and a power-law exponent of 3 and 11. The dashed lines show the heat flow as a function of the square root of dimensionless distance from the left boundary.

exerts a greater drag on the flow, the number of streamlines decreases and a pronounced stagnant region develops below the surface. At the same time, the volume-averaged temperature of the cell, $\langle T \rangle$, increases from 0.5 when $\mu_p = 0$ and $R = 1$, to a maximum of 0.621 when $\log \mu_p = 67.2$ and R is nearly 0. At $\log \mu_p = 67.2$ the non-Newtonian layer is virtually rigid. As the mobility of the non-Newtonian layer decreases, the heat transfer at the upper boundary of the Newtonian layer becomes less and less efficient than at the stress-free lower boundary. As a result, $\langle T \rangle$ must increase in order for the system to achieve steady state. The increased temperatures reduce the rate at which heat enters through the lower boundary, and thus balances the heat flow across the upper and lower boundaries.

5.1.6 Analysis of surface velocity distributions

From the values of R and P obtained for square box calculations ($\Delta = 1$) in the absence of the ridge push force and internal heat generation, four basic regimes of behaviour for the non-Newtonian layer can be defined. These four regimes have the following names and characteristics:

(1) Strong Layer Regime—the average velocity of the non-Newtonian layer is slow with respect to the underlying flow and the surface deformation is distributed.

(2) Strong Plate Regime—the average velocity of the non-Newtonian layer is slow with respect to the underlying flow and the surface velocity is plate-like.

(3) Mobile Plate Regime—the average velocity of the surface non-Newtonian layer is characteristic of the underlying flow and the surface velocity pattern is plate-like.

(4) Mobile Layer Regime—the average velocity of the non-Newtonian layer is characteristic of the underlying flow and the surface deformation is distributed.

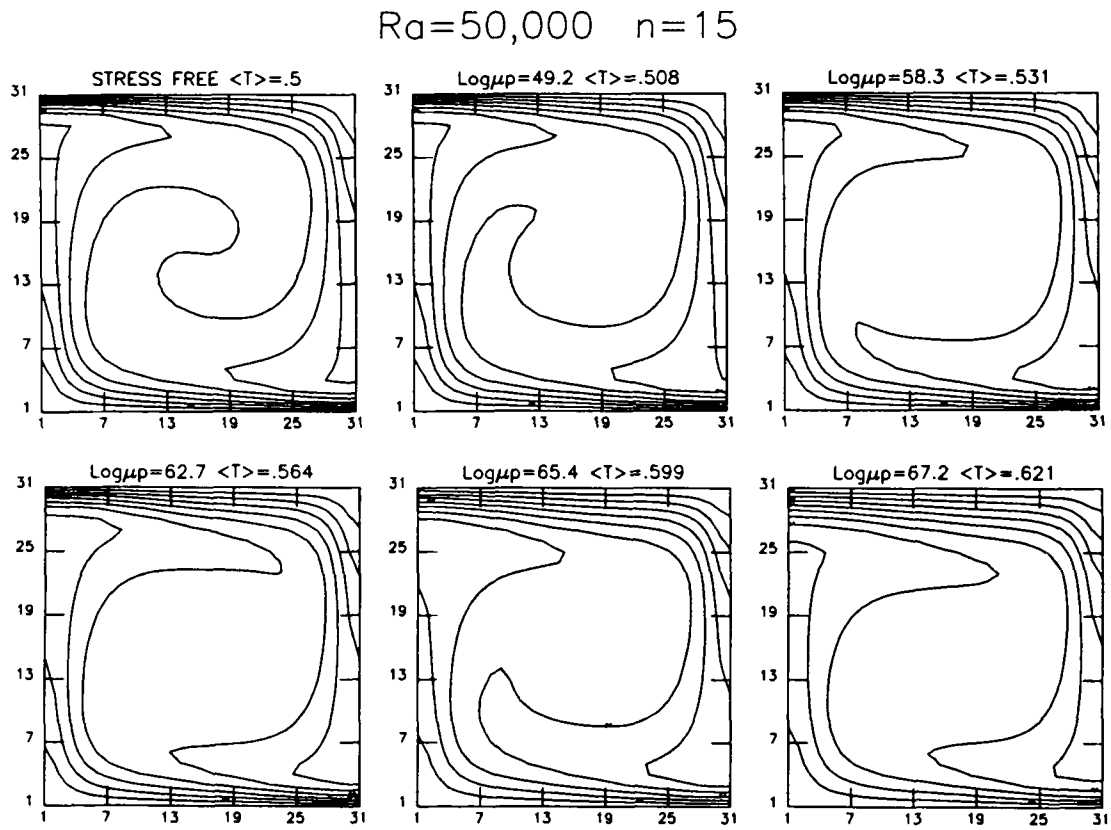

Figure 11. Effects of surface mobility on the temperature field in the Newtonian layer. The numbers along the borders indicate the gridpoints. The volume averaged temperature of the Newtonian layer rises as surface mobility decreases. The contour interval is 0.1.

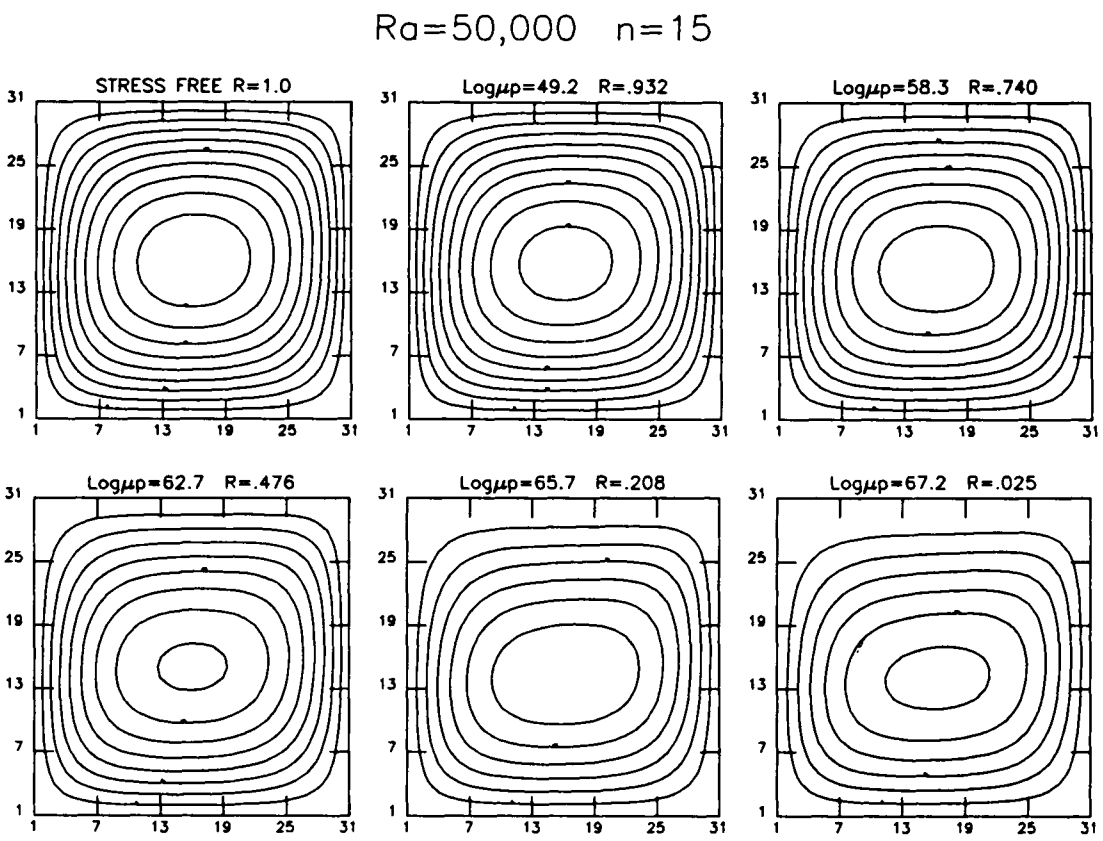

Figure 12. Effects of surface mobility on the momentum field (streamfunction) in the Newtonian layer. The numbers along the borders indicate the gridpoints. The flow becomes less vigorous with decreasing surface mobility. The contour interval is the same for all plots.

Table 2. Regime definitions.

	Regime	R	P
1	Strong Layer	$< .5$	$< .7$
2	Strong Plate	$< .5$	$\geq .7$
3	Mobile Plate	$\geq .5$	$\geq .7$
4	Mobile Layer	$\geq .5$	$< .7$

The R and P values corresponding to these regimes are given in Table 2. Figs 13–15 show regime diagrams for $Ra = 2 \times 10^4$, 2×10^5 and 1×10^6 respectively. These diagrams show the locations of the four plate behaviour regimes in μ_p–n space. At $Ra = 2 \times 10^4$ the mobile plate regime is not encountered in any of the calculations and is therefore not present in Fig. 13. As n decreases to 1, the strong layer regime grows at the expense of strong plate regime for all regime diagrams shown. This behaviour is expected since good plate behaviour does not exist for Newtonian rheology. Neither the strong plate nor mobile plate regimes exist in the case of Newtonian rheology. At $Ra = 2 \times 10^4$ the mobile plate regime probably will not appear until n is increased well above 19, which is the maximum value of n considered in this study. At $Ra = 2 \times 10^5$, the mobile plate regime first appears for $n = 11$ and broadens as n is increased. Note that the strong layer regime is more restricted than it is at $Ra = 2 \times 10^4$. For $Ra = 1 \times 10^6$, the mobile plate regime appears for n as low as 7.

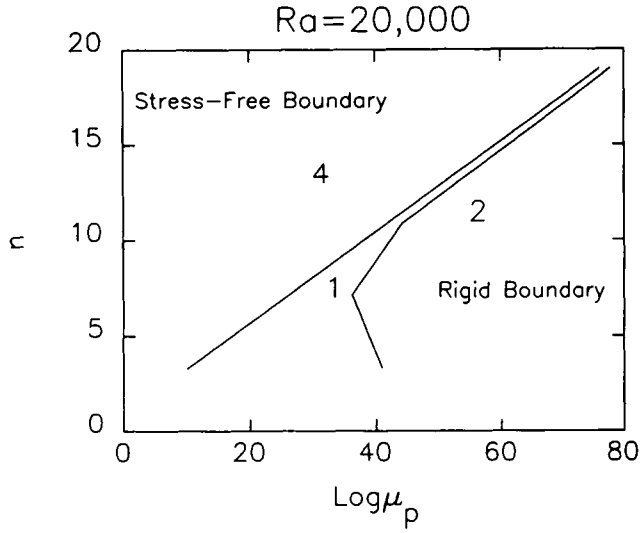

Figure 13. Diagram showing the regimes of behaviour of the non-Newtonian layer when $Ra = 20\,000$. The four regimes are (1) Strong Layer Regime, (2) Strong Plate Regime, (3) Mobile Plate Regime, and (4) Weak Layer Regime. The mobile plate regime is not encountered for $n \leq 19$ at this Rayleigh number.

5.1.7 Steady solutions with internal heating

In this section we examine the effects of internal heating by varying r while leaving the other parameters Ra, n, and μ_p fixed. Fig. 16 shows surface velocity distributions obtained

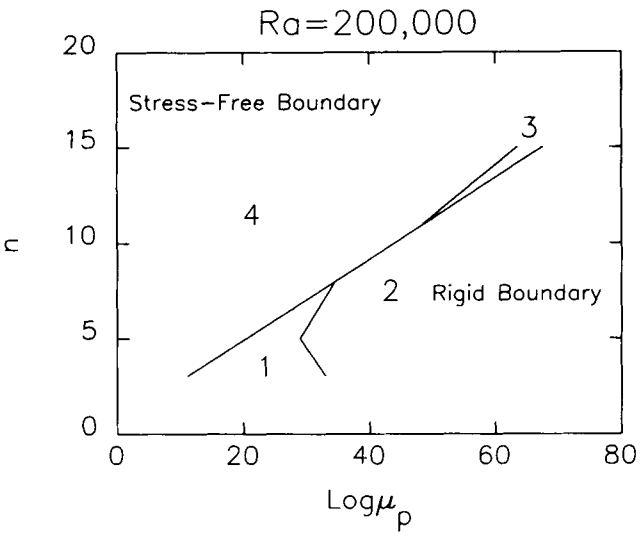

Figure 14. Diagram showing the regimes of the behaviour of the non-Newtonian layer when $Ra = 200\,000$. The four regimes are (1) Strong Layer Regime, (2) Strong Plate Regime, (3) Mobile Plate Regime, and (4) Weak Layer Regime.

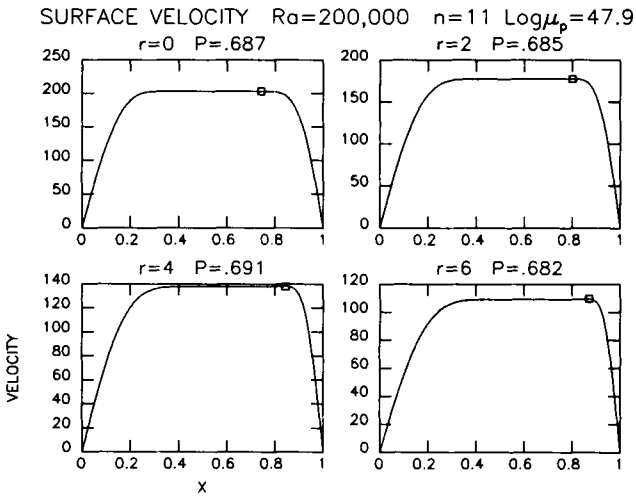

Figure 16. The effects of internal heat generation on the surface velocity distribution. As the amount of internal heating increases, the left margin broadens and the right margin narrows. Only the dimensionless heat source r is varied.

for $Ra = 5 \times 10^4$, $n = 15$, and values for r of 0, 2, 4 and 6. When r is increased, the velocity decreases and the surface velocity distribution becomes more asymmetric as the width of the left margin increases and the width of the right margin decreases. Fig. 17 shows the contoured streamfunction fields corresponding to the surface velocity distributions in Fig. 16. It is clear that the increasing asymmetry of the surface velocity distribution is the result of the asymmetric flow that occurs with $r \neq 0$ in the Newtonian layer. Increasing r has almost no effect on plateness. The shrinking right margin apparently makes up for the broadening left margin.

The normal and shear stress distributions corresponding to the surface velocity distributions in Fig. 16 are displayed in Fig. 18. They also reflect the asymmetry of the convecting flow. As r is increased from zero, the shear stresses on the left side of the cell diminish because the convective upwelling becomes weak and the transition from tensile to compressive stress moves to the right. For large amounts of internal heat generation most of the non-Newtonian layer is in tension.

The rest of the results from the internally heated calculations are presented in Tables 3 and 4. They show the large rise in $\langle T \rangle$ which occurs with internal heating. For $Ra = 5 \times 10^4$ and $r = 6$, $\langle T \rangle = 0.855$ and the values of the surface and basal averaged Nusselt numbers ($\langle Nu \rangle_s$ and $\langle Nu \rangle_b$) indicate that more than 70 per cent of the surface

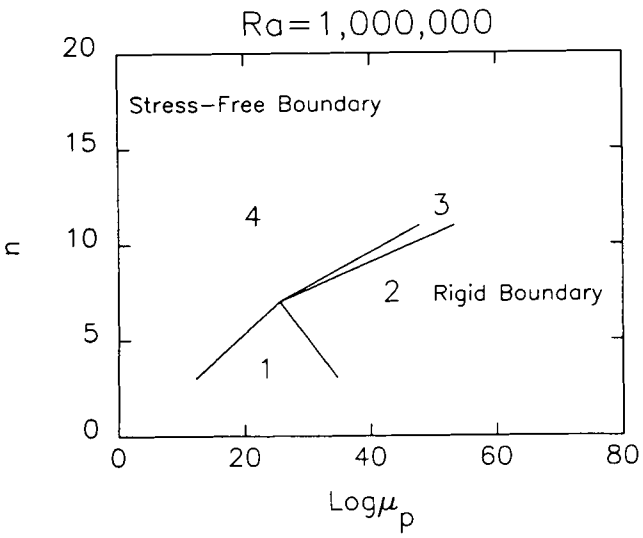

Figure 15. Diagram showing the behaviour of the non-Newtonian layer when $Ra = 1\,000\,000$. The four regimes are (1) Strong Layer Regime, (2) Strong Plate Regime, (3) Mobile Plate Regime, and (4) Weak Layer Regime.

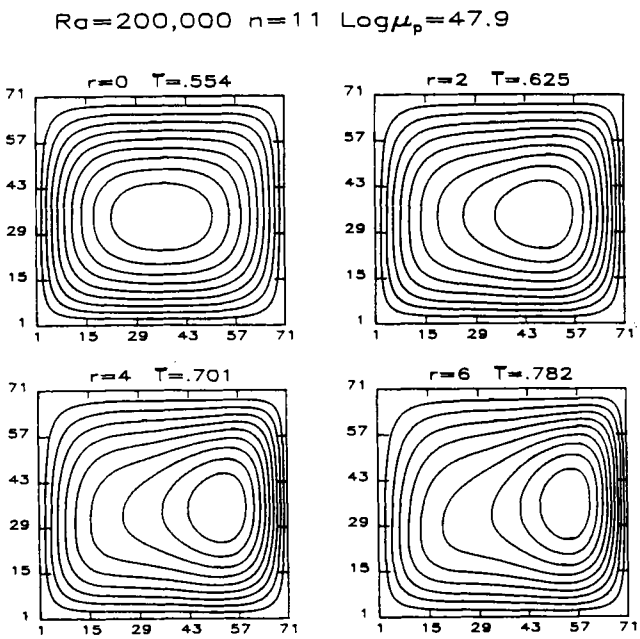

Figure 17. Stream function fields corresponding to the surface velocity distributions in Fig. 16.

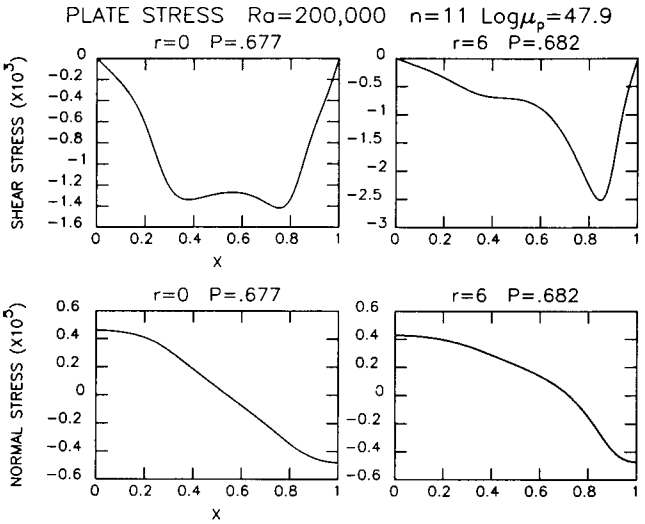

Figure 18. The effects of internal heat generation on the dimensionless shear and normal stress distributions in the non-Newtonian layer. With internal heat generation, the shear stress becomes concentrated over the downwelling and most of the non-Newtonian layer goes into tension.

Table 3. $Ra = 2 \times 10^5$ $r \neq 0$

n	$\log \mu_p$	r	$< T >$	$< Nu >$	$< Nu >_s$	$< Nu >_b$	P	R
15	62.7	0	0.564	6.87	6.87	6.87	0.662	0.476
15	62.7	2	0.658	6.44	7.36	5.36	0.677	0.469
15	62.7	4	0.754	5.90	7.82	3.86	0.676	0.441
15	62.7	6	0.855	5.25	8.16	2.25	0.676	0.391

Table 4. Regime definitions

n	$\log \mu_p$	r	$< T >$	$< Nu >$	$< Nu >_s$	$< Nu >_b$	P	R
11	47.9	0	0.554	11.19	11.19	11.19	0.687	0.621
11	47.9	2	0.625	10.37	11.07	9.04	0.685	0.616
11	47.9	4	0.701	9.18	10.91	6.97	0.691	0.583
11	47.9	6	0.782	8.21	10.96	5.09	0.682	0.538

heat flow is due to internal heat generation. For $Ra = 2 \times 10^5$ and $r = 6$, $\langle T \rangle = 0.782$ and only 54 per cent of the surface heat flow is due to internal heat generation. These tables also show that R decreases as the amount of internal heat generation is increased. Therefore, the presence of internal heating would decrease the width of the mobile plate regime in Figs 13–15.

5.2 The effects of the ridge push force

As the Earth's lithosphere moves away from the mid-ocean ridges, it becomes negatively buoyant and subsides into the mantle. The elevation of the mid-ocean ridges above the sea-floor establishes a pressure head which acts to drive the lithosphere laterally away from the ridges (Hager & O'Connell 1981). This pressure head gives rise to the *ridge push* force, which acts downslope and is parallel to the lithosphere. In this section, we discuss the effects of including the ridge push force in our plate–mantle coupling model.

The ridge push force in dimensional form is

$$F_r = \rho g \frac{\partial \zeta(x)}{\partial x} \hat{x}, \tag{40}$$

where ζ is the surface topography. The ridge push force is simply the derivative in x of the pressure head. The dimensionless surface topography is given by the following expression (McKenzie, Roberts & Weiss 1974; Jarvis & Peltier 1982):

$$\zeta(x) = \left[\int_0^x \frac{\partial \omega_y(s)}{\partial z} \bigg|_{z=1} ds - 2 \frac{\partial w_m(s)}{\partial z} \bigg|_{z=1} \right], \tag{41}$$

since the dynamic topography is the negative of the vertical normal stress, we can write the dynamic non-linear vorticity boundary condition as

$$\omega_y |_{z=1} = h \left[2 \frac{\partial}{\partial x} \left(\eta \frac{\partial u_p}{\partial x} \right) - \frac{\partial \zeta}{\partial x} \right] \bigg|_{z=1}. \tag{42}$$

If the $\partial \zeta(x)/\partial x$ term is negative, then it is possible for the buoyancy of the non-Newtonian plate to drive the flow. Until now, the mass of the plate has been neglected. Implicit in this formulation is the assumption made in Section 3, i.e. the presence of the plate does not alter the buoyancy distribution in the Newtonian layer.

Figs 19–21 show the effects of including the ridge push effect on the surface velocity, shear stress and normal stress distributions respectively. The upper plots in each figure show the results from calculations with the ridge push effect included and lower plots show the results from calculations for the same rheology and value of Ra for the non-Newtonian layer but with the ridge push force absent. Fig. 21 also shows the surface topography ζ for both ridge push calculations. This allows one to estimate the contribution of the ridge push effect to the force balance on the plate.

From Fig. 19, one can see that inclusion of the ridge push effect results in larger R and P. Therefore, with the ridge push effect the non-Newtonian layer becomes more mobile with better plateness. Note that for the calculation with log $\mu_p = 47.9$, $R = 0.94$, indicating that the non-Newtonian layer is travelling near the free plate velocity. In fact, the shear stress becomes positive under the margins of the non-Newtonian layer, indicating that the non-Newtonian

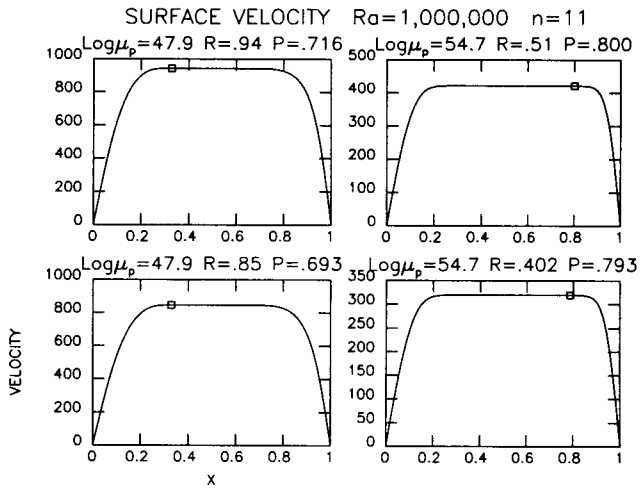

Figure 19. The effects of the ridge push force on the surface velocity distribution. The two upper figures show the velocity distributions when the ridge push force is included. For comparison, the lower figures show the surface velocity distribution when the ridge push force is absent.

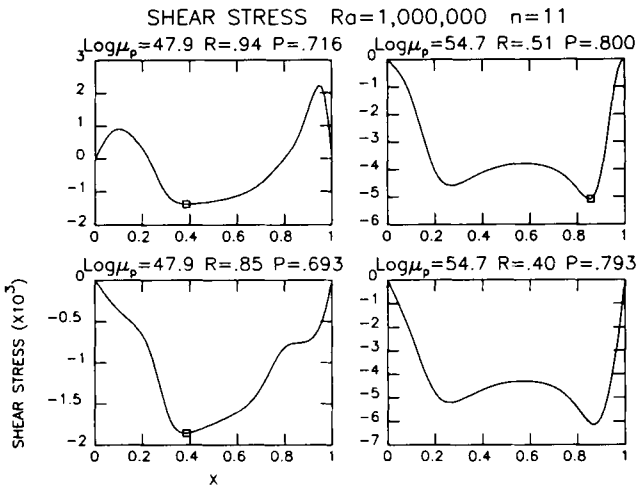

Figure 20. Basal shear stress distributions corresponding to the velocity distributions in Fig. 19. The ridge push force is absent in the lower two figures.

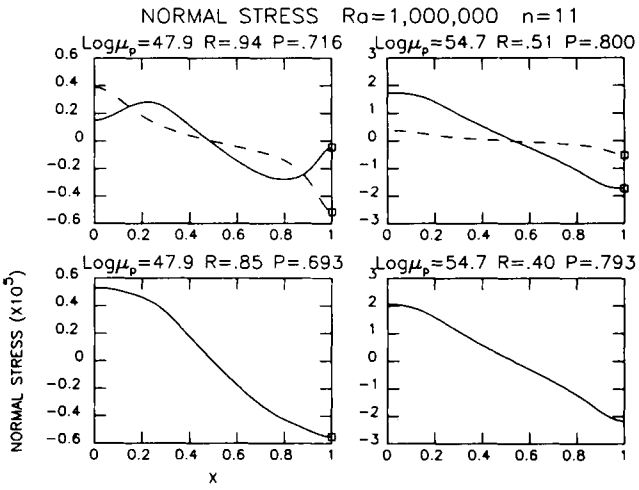

Figure 21. The topography and effects of the ridge push force on the normal stress distribution. The dashed line shows the topography ζ.

layer is driving the flow in these regions. In the case of fast moving plates, the ridge push force may provide the bulk of the driving force. For slower moving plates (Fig. 21, $R = 0.51$), the ridge push force provides only a small fraction ~10 per cent. The transition from tensile to compressive normal stress still occurs near the middle of the cell. The addition of the ridge push force would increase the width of the mobile plate regime in Figs 13–15.

Downwellings in the Newtonian layer *tug* on the non-Newtonian layer through the generation of basal shear stresses. The coupling between the Earth's plates and subducting slabs is different because the slab is an extension of the lithosphere into the mantle. In our model, the non-Newtonian rheology is restricted to a thin layer and does not subduct into the Newtonian fluid. Thus, we cannot properly assess the effects of the slab pull force.

5.3 Non-steady solutions

Figs 22 and 23 show the temperature fields and the corresponding surface velocity distributions obtained from a time-dependent convection calculation where $Ra = 5 \times 10^4$, $n = 15$, $\log \mu_p = 65.4$ and $\Delta = 5$, at dimensionless times 0.025 and 0.05. The initial condition used is a single cell perturbation with top and bottom thermal boundary layers and a mean dimensionless temperature of 0.5. The large aspect-ratio single cell quickly breaks down in to five separate cells. At a dimensionless time of 0.025 there are five cells with different sizes present in the temperature field. The corresponding surface velocity distribution shows the presence of five distinct plates in the non-Newtonian layer. Plates 2 and 4 are travelling to the left towards downwellings in the flow and plates 1, 3 and 5 are travelling

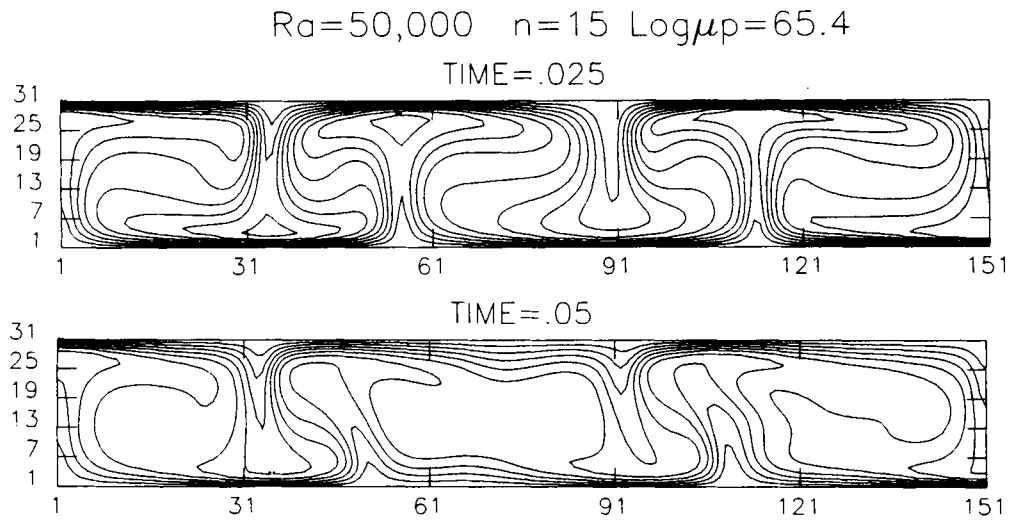

Figure 22. Snapshots of the temperature field of the Newtonian layer obtained from a time-dependent calculation performed using $Ra = 50\,000$ and a power-law exponent of 15. The contour interval is 0.1.

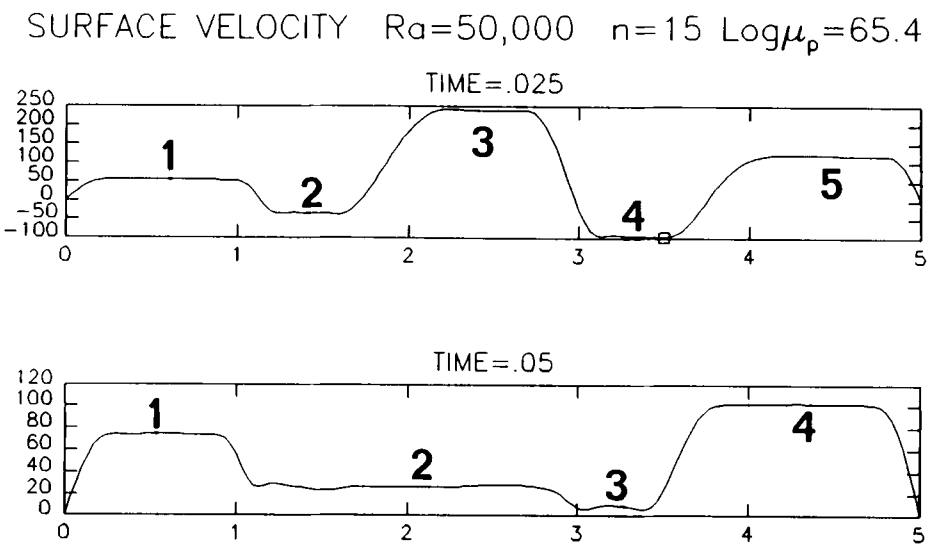

Figure 23. The surface velocity distributions corresponding to the temperature fields in Fig. 22.

to the right away from upwellings. Therefore, spreading centres exist between plates 2 and 3, and plates 4 and 5, and convergent centres exist between plates 1 and 2, and plates 3 and 4.

By a dimensionless time of 0.05 the configuration of the cells has changed. The third and fifth cells have grown at the expense of the second and fourth cells. The dimensions of the first cell have remained approximately unchanged. In the corresponding surface velocity distribution only four distinct plates are present. Shear stresses at the base of the non-Newtonian layer generated by convection in the second cell have become weak enough so that the second cell does not produce a distinct plate and the divergent boundary between plates 2 and 3 present at $t = 0.025$ has disappeared. Therefore by $t = 0.05$ plates 2 and 3 have sutured and the spreading centre between them has vanished. However, the second cell does influence the surface velocity distribution by causing intraplate deformation on the left side of the second plate. The third plate is also experiencing some intraplate deformation. Perhaps at a later time it too will become part of the large plate.

Figures 24 and 25 show the surface heat flow and topography (ζ) corresponding to the temperature fields of Fig. 22. As expected, regions of high topography and heat flow are correlated with convective upwellings and regions of low heat flow and negative topography are associated with convective downwellings. Despite the disappearance of the spreading centre between plates 2 and 3 by a dimensionless time of 0.05, the surface heat flow and topography plots still show high heat flow and topography in this region.

A few results from a time-dependent calculation with internal heat generation are displayed in Figs 26–28. In this calculation, the flow in the Newtonian layer is dominated by cold descending sheets. Compared to the downwellings, the upwellings are essentially passive. The velocity field of the non-Newtonian layer is organized into four plates with two spreading centres and three centres of convergence. The tensile stresses responsible for the spreading centres are not generated by the nearly passive upwellings, but by the cold downwellings on either side. The basal shear stress distribution (Fig. 28) shows that only a small amount of drag

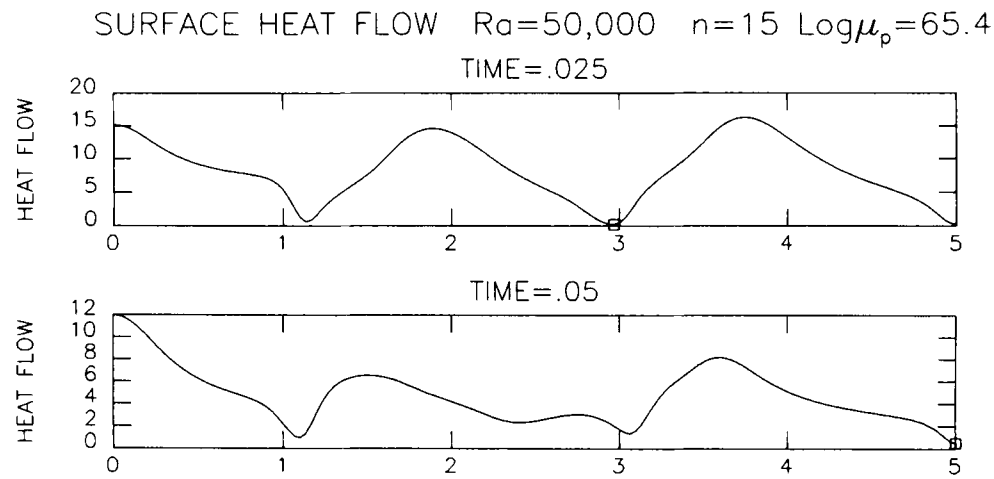

Figure 24. The surface heat flow distribution calculated from the temperature fields in Fig. 22.

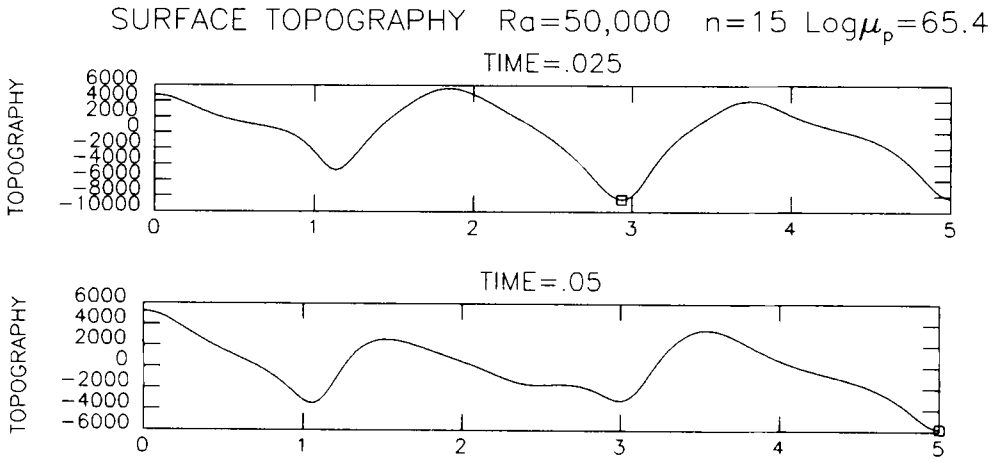

Figure 25. The surface topography ζ corresponding to the temperature fields in Fig. 22.

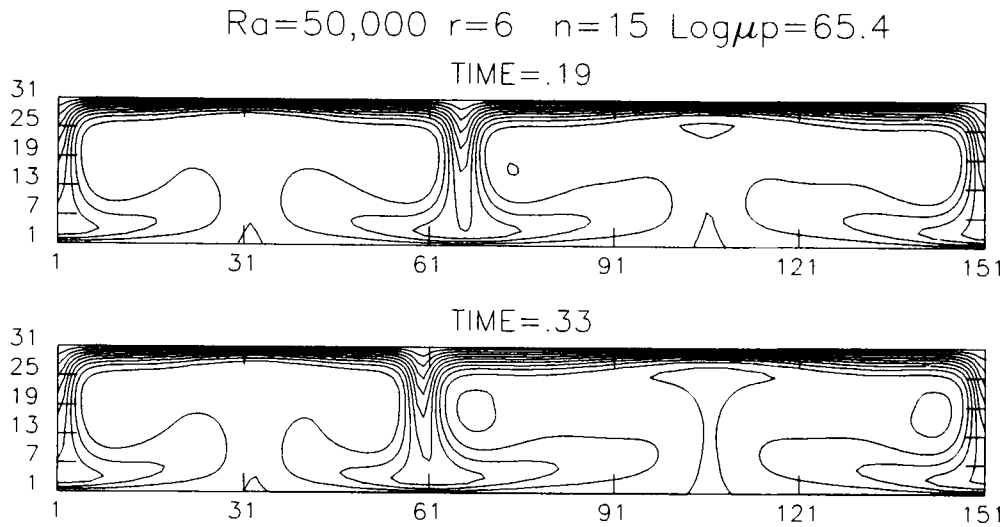

Figure 26. Snapshots of the temperature field of the Newtonian layer obtained from a time-dependent calculation performed using $Ra = 50\,000$, $r = 6$ and a power-law exponent of 15. The contour interval is 0.1.

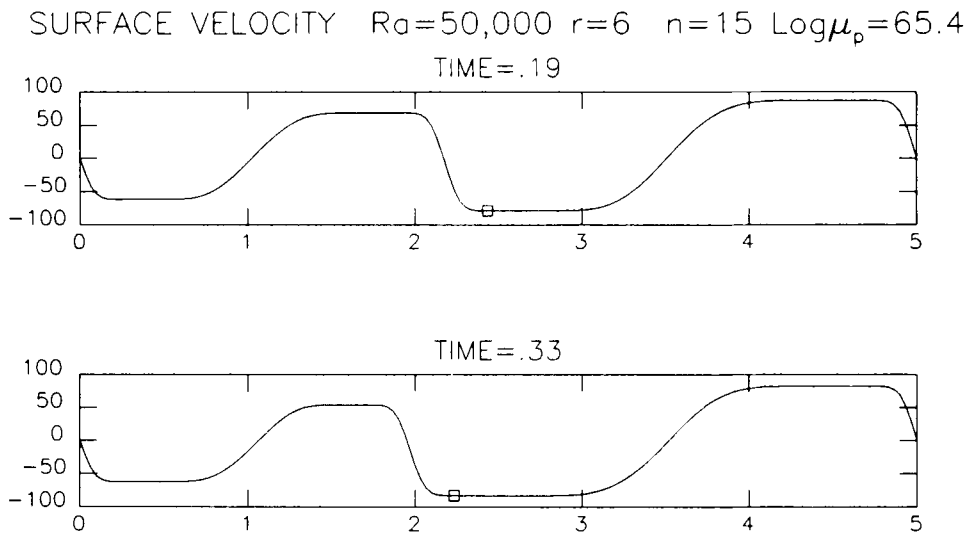

Figure 27. The surface velocity distributions corresponding to the temperature fields in Fig. 26.

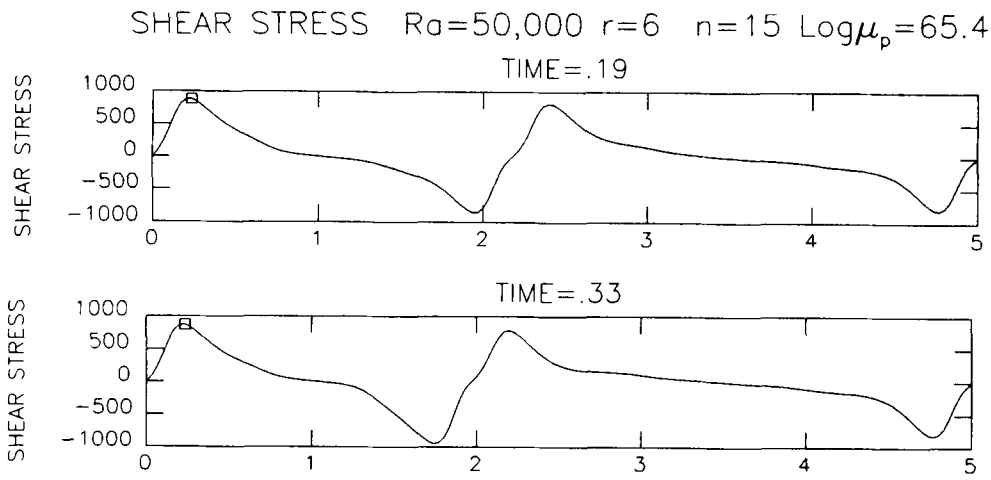

Figure 28. The basal shear stress distributions corresponding to the temperature fields in Fig. 26. The shear stresses are small over the weak upwellings in the Newtonian layer.

is generated by the upwellings. The spreading centres in this calculation are passive; they are not the result of strong upwellings in the Newtonian layer.

6 CONCLUSIONS

The results from the analysis of the surface velocity distributions produced by the plate–mantle coupling model show that the deformation in the non-Newtonian layer is distributed (low plateness) when the values of μ_p or n are small. The surface velocity distributions with large values of plateness ($P > 0.7$) are qualitatively similar to those found in Christensen (1984), which used $n = 3, 5$ and Christensen & Harder (1990), which used $n = 6$. In these studies, the entire convecting layer is assumed to have a non-Newtonian rheology, not just a thin layer at the top. In our model, mobile plate-like behaviour is found only when $n \geq 7$, which is substantially higher than the values of n (3.0–3.5) typically found in creep experiments on olivine (Weertman & Weertman 1975; Goetze 1978; Durham, Froidevaux & Jaoul 1979). It is known from seismic and marine studies that mid-ocean ridges contain active listric normal faults. These faults may help confine the deformation in the lithosphere closer to the ridge. Thus the microphysical power law may be enhanced by macroscopic effects such as faulting. A conclusion that may be drawn from this study is that the rheology of the lithosphere must be strongly non-linear. Future work which will assess the effects of changing plate thickness and temperature dependent μ_p could conceivably find a lower value of n needed for mobile plate-like behaviour.

Our model has a few implications for the state of stress and force balance in oceanic lithosphere. In the simplest calculations where internal heating and the ridge push force are not included, the transition from tensile to compressive stress occurs halfway across the non-Newtonian layer. When large amounts of internal heating are present, most of the non-Newtonian layer is in deviatoric extension. The inclusion of the ridge push force results in larger velocities, lower basal shear stresses and better plate-like characteristics of the non-Newtonian layer. However, the ridge push force has little effect on the basic distribution of the normal stress; the transition from tensile to compressive stress still occurs approximately halfway across the non-Newtonian layer. We find the ridge push force to be of most importance for fast moving plates, where it provides most of the driving force.

In general the normal stress distributions found in this study are quite different from those obtained by Wiens & Stein (1985), which predicts the oceanic lithosphere is in deviatoric compression. Wiens & Stein (1985) applied two constraints in determining the normal stress field $\langle \sigma_{xx} \rangle_v$. One constraint requires $\langle \sigma_{xx} \rangle_v$ to vanish at the ridge (weak ridge condition) and the other requires that old lithosphere be in deviatoric compression. This model was used to explain the observation (Wiens & Stein 1984) that intraplate earthquakes, especially those occurring in old lithosphere, tend to have thrust fault mechanisms. In our model, the velocity at the ridge vanishes, and the ridge has the same rheology as the rest of the lithosphere. The divergent boundaries produced in our plate–mantle coupling model are weak precisely because $\langle \sigma_{xx} \rangle_v$ is large there.

While the Wiens & Stein (1985) model can account for the prevalence of thrust fault mechanisms among large intraplate events, it does not predict ridge seismicity. In the context of our model, either intraplate seismicity is not a reliable indicator of the general state of stress in oceanic lithosphere or the current catalogue of intraplate events is too small to be statistically meaningful.

The time-dependent calculations discussed in Section 5.3 demonstrate the ability of the plate-coupling model to adjust the number of plates, their speeds and their geometries depending on the convective flow in the Newtonian layer. These calculations show that the pattern of surface motion will not always mirror the pattern of convection. In the limit, where the non-Newtonian layer is weak, there will be a one-to-one correspondence between the divergences in the surface velocity field and the vertical flows in the Newtonian layer. As the non-Newtonian layer is made stronger, this correspondence will degrade and vanish altogether if the non-Newtonian layer is made rigid. Our calculations support the possibility that ridges simply represent the locus of large tensile stresses in the lithosphere (Turcotte & Oxburgh

1973), and not the location of mantle upwellings. Seismological evidence suggests that subducting lithosphere extends to at least the 670 km discontinuity, and in some cases probably beyond (Creager & Jordan 1986; Dziewonski & Woodhouse 1987; van der Hilst *et al.* 1991). Therefore subduction zones should be associated with downwellings in the mantle. On the other hand, tomographic studies such as Dziewonski & Woodhouse (1987) and Tanimoto & Zhang (1991) indicate the ridges may not be associated with strong upwellings from the deep mantle. An analogous situation is found in our model when internal heat generation is strong. In this case, cold descending sheets dominate the flow in the Newtonian layer and passive spreading centres are produced between them.

ACKNOWLEDGMENTS

S.A. Weinstein was supported by a grant from the UCRP of IGPP at LANL. The authors thank Dave Yuen and the Minnesota Supercomputer Institute for use of their computational facilities. The authors also appreciate helpful reviews by S. D. King and Y. Chen. S.A.W. is indebted to Neil Ribe for valuable discussions.

REFERENCES

Chase, C. G., 1978. Plate Kinematics: the Americas, East Africa and the rest of the World, *Earth planet. Sci. Lett.*, **37,** 355–368.

Chen, Y. & Morgan, J. W., 1990. A non-linear rheology model for mid-ocean ridge axis topography, *J. geophys. Res.*, **95,** 17 583–17 604.

Christensen, U. R., 1983. Convection in a variable viscosity fluid: Newtonian versus power law, *Earth planet. Sci. Lett.*, **64,** 153–162.

Christensen, U. R., 1984. Convection with pressure and temperature dependent non-Newtonian rheology, *Geophys. J. R. astr. Soc.*, **77,** 343–384.

Christensen, U. R. & Harder, H., 1991. 3-D convection with variable viscosity, *Geophys. J. Int.*, **104,** 213–226.

Creager, K. C. & Jordan, T. H., 1986. Slab penetration into the lower mantle beneath the Mariana and other island arcs of the northwest Pacific, *J. geophys. Res.*, **91,** 3572–3589.

Cserepes, L., 1982. Numerical studies of non-Newtonian mantle convection, *Phys. Earth planet. Inter.*, **30,** 49–61.

Davies, G. F., 1988. Role of the lithosphere in mantle convection, *J. geophys. Res.*, **93,** 10 451–10 466.

Davies, G. F., 1989. Mantle convection model with a dynamic plate: topography, heat flow and gravity anomalies, *Geophys. J. Int.*, **98,** 461–464.

DeMets, C., Gordan, R. G., Argus, D. F. & Stein, S., 1990. Current plate motions, *Geophys. J. Int.*, **101,** 425–478.

Durham, W. B., Froidevaux, C. & Jaoul, O., 1979. Transient and steady state creep of pure fosterite at low stress, *Phys. Earth planet. Inter.*, **19,** 263–274.

Dziewonski, A. M. & Woodhouse, J. H., 1987. Global images of the Earth's interior, *Science*, **236,** 37–48.

Goetze, C., 1978. The mechanism of creep in olivine, *Phil. Trans. R. Soc. Lond. A.*, **288,** 99–119.

Gurnis, M., 1988. Large-scale mantle convection and the aggregation and dispersal of supercontinents, *Nature*, **332,** 695–699.

Gurnis, M. & Hager, B. H., 1988. Controls of the structure of subducted slabs, *Nature*, **335,** 317–321.

Hager, B. H. & O'Connell, R. J., 1981. A simple global model of plate dynamics and mantle convection, *J. geophys. Res.*, **86,** 4843–4867.

Jarvis, G. T. & Peltier, W. R. 1982. Time-dependent convection in the Earth's mantle, *Phys. Earth planet. Inter.*, **36,** 305–327.

King, S. D. & Hager, B. H., 1990. The relationship between plate velocity and trench viscosity in Newtonian and power-law subduction calculations, *Geophys. Res. Lett.*, **12,** 2409–2412.

Kopitzke, U., 1979. Finite element convection models: comparison of shallow and deep mantle convection and temperatures in the mantle, *J. Geophys.*, **46,** 97–121.

McKenzie, D. P., Roberts, J. M. & Weiss, N. O., 1974. Convection in the Earth's mantle: towards a numerical simulation, *J. Fluid Mech.*, **62,** 465–538.

Minster, J. B. & Jordan, T. H., 1978. Present-day plate motions, *J. geophys. Res.*, **83,** 5331–5354.

Olson, P. & Corcos, G. M., 1980. A boundary layer model for mantle convection with surface plates, *Geophys. J. R. astr. Soc.*, **62,** 195–219.

Parsons, B. & Sclater, J. G., 1977. An analysis of the variation of ocean floor bathymetry and heat flow with age, *J. geophys. Res.*, **82,** 803–827.

Ribe, N., 1992. The dynamics of thin shells with variable viscosity and the origin of toroidal flow in the mantle, *Geophys. J. Int.*, 537–552.

Stocker, R. L. & Ashby, M. F., 1973. On the rheology of the upper mantle, *Rev. Geophys. Space Phys.*, **11,** 391–426.

Tanimoto, T. & Zhang, Y., 1991. Deciphering active vs. passive upwellings from depth of low velocity anomalies, *EOS Trans. Am. geophys. Un.*, **72,** 277.

Turcotte, D. L. & Oxburgh, E., 1973. Mid-plate tectonics, *Nature*, **244,** 337–339.

van der Hilst, R., Engdahl, R., Spakman, W. & Nolet, G., 1991. Tomographic imaging of subducted lithosphere below northwest Pacific island arcs, *Nature*, **353,** 37–43.

Weertman, J., 1970. The creep strength of the Earth's mantle, *Rev. Geophys. Space Phys.*, **8,** 146–168.

Weertman, J. & Weertman, J. R., 1975. High temperature creep of rock and mantle viscosity, *Ann. Rev. Earth planet. Sci.*, **3,** 293–316.

Weinstein, S. A., Olson, P. & Yuen, D. A., 1989. Time-dependent large aspect-ratio convection in the Earth's mantle, *Geophys. Astrophys. Fluid Dyn.*, **47,** 157–197.

Wiens, D. A. & Stein, S., 1984. Intraplate seismicity and stresses in young oceanic lithosphere, *J. geophys. Res.*, **89,** 11 442–11 464.

Wiens, D. A. & Stein, S., 1985. Implications of oceanic intraplate seismicity for plate stresses, driving forces and rheology, *Tectonophysics*, **116,** 143–162.

Zhang, Y. & Tanimoto, T., 1992. Ridge hotspots and their interactions observed in seismic velocity maps, *Nature*, **355,** 45–49.